

# Physical conditions around high-mass young star-forming objects via simultaneous observations of excited OH and methanol masers

A. Kobak<sup>1</sup> , A. Bartkiewicz<sup>1</sup> , K. L. J. Rygl<sup>2</sup> , A. M. S. Richards<sup>3</sup> , M. Szymczak<sup>1</sup> , and P. Wolak<sup>1</sup> 

<sup>1</sup> Institute of Astronomy, Faculty of Physics, Astronomy and Informatics, Nicolaus Copernicus University, Grudziadzka 5, 87-100 Torun, Poland

<sup>2</sup> INAF-Istituto di Radioastronomia, Via P. Gobetti 101, I-40129, Bologna, Italy

<sup>3</sup> JBCA, Department of Physics and Astronomy, University of Manchester, UK

Received 2024 / Accepted 2024

## ABSTRACT

*Context.* Astrophysical masers are widely used in star formation studies. In particular, they are valuable in investigations of high-mass star-forming regions that are difficult to observe at optical frequencies.

*Aims.* We used multi-transition data to derive physical conditions in the immediate environment of forming high-mass stars.

*Methods.* Simultaneous observations of two maser transitions, excited OH at 6.035 GHz and methanol at 6.668 GHz, were made using e-Merlin. Both transitions are radiatively pumped but prefer diverse physical conditions.

*Results.* We imaged ten high-mass star-forming sites with milliarcsecond angular resolution, identifying regions where excited OH and methanol masers coexist and where they avoid each other. Moreover, we identified circularly polarized Zeeman splitting pairs of the OH transition, estimating magnetic field strengths in the range from 0.2 to 10.6 mG. The detection of linearly polarized components enabled us to compare the directions of magnetic field vectors with the outflows coming from the young star-forming objects.

*Conclusions.* We found that the two maser lines appeared to coexist in six high-mass star-forming regions, in cloudlets separated by up to 205 au. Where the lines show avoidance, this can be related to changes in dust and gas temperatures; we also found a few examples suggestive of a high gas density. In seven sources, Kolmogorov-Smirnov tests show the nonrandom relationship between the position angles of distribution of the two maser transitions. We did not obtain consistent results regarding the direction of the magnetic field and outflow.

**Key words.** masers – stars: massive – stars: formation – polarization – ISM: magnetic fields – ISM: molecules

## 1. Introduction

Astrophysical masers are used to study high-mass young star-forming objects (HMYSOs), in particular maser emission from hydroxyl (OH), water (H<sub>2</sub>O), and methanol (CH<sub>3</sub>OH) molecules. In this publication, we focus on two maser transitions: excited OH at 6.035 GHz (hereafter ex-OH) and methanol at 6.668 GHz (hereafter 6.7 GHz). Both are excited via thermal, infrared emission from warm dust that is heated by nearby protostars and may or may not occur in the same volume of gas, depending on the physical conditions, as was modeled in Cragg et al. (2002). The OH radical is a paramagnetic molecule; therefore, Zeeman splitting can be observed from the left- and right-hand circularly polarized (LHCP and RHCP) spectra, and the strength and direction of the magnetic fields can be derived from the separations of both features in the velocity domain (e.g., Avison et al. 2016, Szymczak et al. 2020, Ouyang et al. 2022). If a third, linearly polarized component is detected at the central, unshifted velocity, a Zeeman triplet is identified (e.g., Hutawarakorn et al. 2002; Green et al. 2015). As methanol is diamagnetic, the Zeeman splitting is much smaller and requires very high angular and velocity resolution for detection (e.g., Vlemmings et al. 2011, Surcis et al. 2012, Surcis et al. 2013, Surcis et al. 2015, Surcis et al. 2019, Surcis et al. 2022). Observations and modeling show that the 6.7 GHz transition is the brightest methanol maser under a wide range of physical conditions,

such as a kinetic temperature of 30–150 K, appearing at dust temperatures above 100 K and diminishing when the gas temperature approaches or exceeds the dust temperature. The excitation of the 6.7 GHz methanol maser requires a hydrogen number density,  $n$ , in the range from  $10^5$  to  $10^{8.3}$  cm<sup>-3</sup>; the brightness temperature is independent of  $n$  up to  $10^8$  cm<sup>-3</sup> and above this value falls abruptly (Cragg et al. 2002). The 6.035 GHz OH emission arises from a main-line excited-state transition and appears at lower gas temperatures. It is quenched at a kinetic temperature above 70 K, and is independent of dust temperature. The ex-OH line is also related to high-number-density conditions, extending up to  $10^{8.5}$  cm<sup>-3</sup> with a maximum brightness temperature in the range from  $10^7$  to  $10^8$  cm<sup>-3</sup> (Cragg et al. 2002).

The morphology and kinematics, including proper motion studies, of the methanol maser at 6.7 GHz in HMYSOs have been relatively broadly examined (e.g., Bartkiewicz et al. 2009, 2014, 2016, 2020, 2024, Goddi et al. 2011, Moscadelli et al. 2011, Pandian et al. 2011, Sanna et al. 2010a,b, Sugiyama et al. 2008). Still, it is not clear where exactly 6.7 GHz methanol masers arise. In a few cases, the 6.7 GHz maser reveals a ring-like morphology (Bartkiewicz et al. 2009), which may indicate a disk seen face-on or an outflow oriented along the line of sight (Bartkiewicz et al. 2005). However, detailed studies have shown that complex scenarios are common, in which the masers kinematics can result from a combination of rotation and expansion (Bartkiewicz et al. 2024). Sugiyama et al. (2011) measured the

proper motions of 6.7 GHz maser spots around the well-known HMYSO ON1 and concluded that the internal motions either traced the expanding ultracompact H<sub>II</sub> region or were associated with a molecular outflow. In HMYSO G23.01–0.41, the velocity field of methanol masers was explained in terms of a combination of slow radial expansion with rotation about an axis approximately parallel to the maser jet (Sanna et al. 2010b).

In the case of ex-OH masers, far fewer regions have been imaged in this transition, and they tend to be more compact relative to the methanol masers, preventing a detailed discussion of the kinematic structures in general (e.g., Desmurs et al. 1998; Desmurs & Baudry 1998; Etoke et al. 2012). The first untargeted survey of ex-OH, covering the Galactic longitude ranges  $186^\circ < l < 60^\circ$ , including the Galactic center, reported the detection of 127 sources, which is around 10% of the number of sources with 6.7 GHz methanol masers found in this region (Avison et al. 2016). In general, ex-OH masers are weaker than methanol masers, with brightness temperatures as much as two orders of magnitude lower. This statistic was confirmed by Szymczak et al. (2020), when they surveyed a sample of 445 HMYSOs, identified by the 6.7 GHz methanol transition, and detected 37 ex-OH targets, using the Torun 32-m radio telescope. Due to the small number of imaged regions, it is still uncertain where the ex-OH masers arise. They can be related to a disk, an outflow as well as an intermediate regions. Ex-OH masers may occur in the same place as ground-state (1.665 and 1.667 GHz) OH masers. The latter can trace a dense molecular disk (Hutawarakorn et al. 2002). However, Caswell & Green (2011) present a case in which the ground-state OH emission arises in a fast-moving outflow.

Multi-transition studies of maser emission are valuable in constraining the physical conditions in the gas around HMYSOs. Fish & Sjouerman (2007) used the European VLBI Network and presented the distributions of ex-OH in the HMYSO W3(OH) compared with ground-state OH masers. The ex-OH masers trace the inner edge of a counterclockwise rotating torus of dense molecular gas, while the ground-state OH occurs predominantly to the west of this edge. The 1.667 GHz transition is generally associated with the ex-OH transition, but the 6.0 GHz masers may also appear without the presence of the 1.667 GHz masers. In contrast, 1.665 MHz transition is ubiquitous and can appear separately as well as in association with the ex-OH transition. Identified Zeeman pairs provided estimates of the magnetic field strength of a few milligauss and revealed a reversal of the line-of-sight direction of the magnetic field, oriented away from the observer in the west and toward the observer in the east. Green et al. (2007) imaged the 6.7 GHz methanol and ex-OH lines toward the HMYSO ON1 using MERLIN. Toward the southern part of the ultracompact (UC) H<sub>II</sub> region, the two masers were observed to present a spatial distribution elongated perpendicular to the large-scale bipolar outflow. The Zeeman pairs identified in ex-OH implied the existence of a magnetic field oriented toward the observer with a strength of up to 5.8 mG. The first tentative detection of Zeeman splitting in the 6.7 GHz methanol line was roughly consistent with the above value being  $-18 \pm 6$  mG (a negative value corresponds to the direction pointing toward the observer). Global VLBI observations toward the same target revealed that ex-OH masers have a distribution similar to that of the ground-state OH masers, in contrast to the situation in W3(OH), and this suggests the absence of the highest-density knots in ON1 (Fish & Sjouerman 2010).

This project aims to derive the physical conditions in a sample of HMYSOs via combined observations of ex-OH and methanol masers. In fact, the spatial coincidence or avoidance of

these two masers implies specific physical conditions following the maser excitation models of Cragg et al. (2002). Moreover, the ex-OH maser observations provide: 1) the identification of Zeeman splitting, and thus estimates of the magnetic field strength, and 2) the detection of linearly polarized emission and estimation of the orientation of the magnetic field. This allows us to map the magnetic field structure in the close surroundings of HMYSOs. The continuum emission and methanol polarization will be reported in a future article.

## 2. Observations, data reduction, and methods

The source sample has been chosen based on a large survey of ex-OH carried out since 2018 with the Torun 32 m telescope (Szymczak et al. 2020). Among the 37 detections, we selected 10 sources in which the ex-OH line has a relatively strong (above 1.7 Jy) and non-variable flux density, as was found during two epochs of the survey (November–December 2018 and March–April 2019). In addition, our single-dish studies showed that the spectral features of the 6.7 GHz methanol and ex-OH maser transitions appear at similar LSR velocities.

The observations were made using the enhanced Multi-Element Remotely Linked Interferometer Network (e-MERLIN)<sup>1</sup>, an array of six radio telescopes with baselines between 10–217 km (Garrington & Beswick 2016), under the project CY10206 in July–October 2020 and August 2022. All observations were recorded in full polarization (RR, RL, LR, LL, where R and L represent right- and left-handed circular polarization), and averaged to 4-sec integrations. We observed the masers in two separate sets of spectral tunings, one set covering the ex-OH line (6035.092 MHz) and the other the methanol line (6668.519 MHz). In each tuning, the line was covered by a narrow spectral window 1 MHz wide, consisting of 512 channels with a separation of  $0.1 \text{ km s}^{-1}$ . Each observation was made at constant frequency. Four wide-band ( $\sim 0.13$  GHz each) spectral windows were also observed in the frequency ranges of 6.00–6.51 GHz and 6.30–6.81 GHz (for the ex-OH and methanol tunings, respectively). For each individual source, the ex-OH and methanol tunings were interleaved, changing frequencies every few hours to ensure as near-simultaneous observations as was practical. In some cases, different targets were also interleaved to optimize visibility plane coverage. The list of sources with their phase calibrators, total on-source time, and the central local standard of rest (LSR) velocities is given in Table 1. J1331+3030 (3C286) was observed as a flux and polarization angle standard. J0319+4130 (3C84) and J1407+2827 (OQ208) were observed as bandpass calibrators.

The data were processed using the e-MERLIN CASA 5.8 pipeline (Moldon 2021). The e-MERLIN pipeline includes time- and frequency-dependent calibration of the wide-band data, including estimating the flux scale in janskys and deriving corrections from the phase calibrator source. We calibrated the narrow-band data using CASA 5.8 (McMullin et al. 2007). The first step was flagging any remaining bad data. Then, we used the bandpass calibrator 3C84 to calculate corrections for the phase offset between the wide- and narrow-band data and applied these to the narrow-band 3C84 data, along with the pipeline time-dependent wide-band delay, phase, and amplitude corrections. Next, we performed frequency-dependent calibration to derive a bandpass correction table for amplitude and phase. For ex-OH

<sup>1</sup> e-MERLIN is a National Facility operated by the University of Manchester at Jodrell Bank Observatory on behalf of STFC. <https://www.e-merlin.ac.uk/>

Table 1: Details of eMERLIN observations.

Source name (l b) ( $^{\circ}$ $^{\circ}$ )	Phase Calibrator	Number of scans		Total time on source		Center Vlsr	
		exOH	meth	exOH (h:m)	meth (h:m)	exOH ( $\text{km s}^{-1}$ )	meth ( $\text{km s}^{-1}$ )
G20.237+0.065	J1818–1108	8	8	00:56	00:56	72.3	64.2
G24.148–0.009	J1825–0737	9	6	01:03	00:42	16.7	9.5
G25.648+1.049	J1827–0405	8	8	00:56	00:56	37.4	29.6
G34.267–0.210	J1858+0313	33	33	03:18	03:18	58.0	49.8
G43.149+0.013	J1922+0841	33	33	03:18	03:18	13.5	5.2
G48.990–0.299	J1922+1530	10	10	01:10	01:10	56.4	48.3
G49.490–0.388	J1924+1540	10	10	01:10	01:10	43.7	36.8
G69.540–0.976	J2010+3322	12	12	01:24	01:24	–8.7	–16.4
G81.871+0.781	J2018+3851	18	18	02:06	02:06	11.9	3.7
G108.766–0.986	J2301+5706	13	12	01:31	01:24	–66.0	–73.9

observations, we also derived corrections for polarization leakage (using 3C84, assumed to be unpolarized) and polarization angle by setting the Stokes parameter polarization flux densities for 3C286 for the known position angle (PA) of  $33^{\circ}$  (Perley & Butler 2013).

Next, we applied the narrow-band bandpass calibration, the offset correction, the phase calibrator solutions, and, when applicable, the polarization calibration to the narrow-band target data. We split out the corrected target data, adjusting to constant velocity (LSR, radio convention, relative to the rest frequency of the line) in the target frame. Lastly, we self-calibrated each target using a selected bright channel; for ex-OH, we took care to preserve the relative flux densities in RR and LL, and thus the accuracy of Stokes  $V$  (Green et al. (2007); Darwish et al. (2020), as implemented in CASA). We applied the solutions to all narrow channels and made spectral image cubes for each target (in full polarization, for ex-OH). Using uniform weighting to optimize resolution, the nominal 2-D Gaussian fits to the dirty beam varied from  $121 \times 26$  mas at the lowest declination to  $54 \times 20$  mas for the higher-declination targets (the long axis being close to N-S for the low-declination sources). Since the e-MERLIN beam is quite irregular, we used an intermediate weighting (robust 0.5) and a standard restoring beam of  $65 \text{ mas} \times 45 \text{ mas}$  at a PA of  $-50^{\circ}$ , which has a slightly larger area than the nominal beam fits. This minimizes sidelobe artifacts and makes it easier to compare the images. Since we use component fitting to make measurements, the exact beam shape does not affect the results.

We used the JMFIT procedure in AIPS (NRAO 2022; Greisen 2003) to fit 2D Gaussian components to Stokes  $I$  (total intensity) maser spots for both the methanol and ex-OH masers, and thus measured the positions and the peak flux densities. In addition, using the positions of the  $I$  Stokes ex-OH maser spots, we measured their  $Q$  and  $U$  Stokes parameters as well as the LHCP and RHCP. For further analysis, we took only those spots with a total intensity above  $2\sigma$  that appear in at least two consecutive channels. Table 2 lists the root mean square (rms) for all cubes measured in channels without emission.

Tables 3 and 4 summarize the properties of the brightest maser spot in each source: the absolute coordinates (RA, Dec), the LSR velocity ( $V_p$ ), and the peak flux density ( $S_p$ ). The astrometric accuracies presented in both tables were calculated following the procedure described in Richards et al. (2022): 1) the uncertainty ( $\delta_1$ ) of the position of the phase calibrator, taken from VLBA Catalog<sup>2</sup>, 2) the positional errors ( $\delta_2$ ) due to the image rms noise, calculated for the weakest spots to get their upper

limits, 3) phase errors ( $\delta_3$ ) due to the phase-calibrator and target separation (including the time difference and the angular separation); values of  $\delta_3$  range from 12 to 81 mas, due to variations in atmospheric conditions, and 4) the antenna position errors ( $\delta_4$ ) – we assume a typical baseline error of 2 cm. The total astrometric accuracy is  $\delta_{\text{tot}} = (\delta_1^2 + \delta_2^2 + \delta_3^2 + \delta_4^2)^{0.5}$ .

For the analysis of the coexistence of both maser transitions, we presumed that the lines coincide when: i) Their spectral features at least partially overlie each other in the LSR velocity range; we analyzed both polarizations of ex-OH to take into account the Zeeman splittings on this emission (see an example in Fig. 1). In the case of methanol emission, we neglected the splitting of the two polarizations due to the magnetic field, since its value is significantly smaller (less than one tenth) than the width of one spectral channel. ii) The angular separation between methanol and ex-OH spots is less than  $0.5(\gamma_{6.7} + \gamma_{6.035})$ , where  $\gamma$  is calculated as  $(\delta_2^2 + \delta_3^2)^{0.5}$  for both transitions, respectively. Since we compare observations made with the same phase calibrator and antennas, we do not need to consider errors  $\delta_1$  and  $\delta_4$ . The values of  $\gamma$  are listed in Tables 3 and 4, respectively.

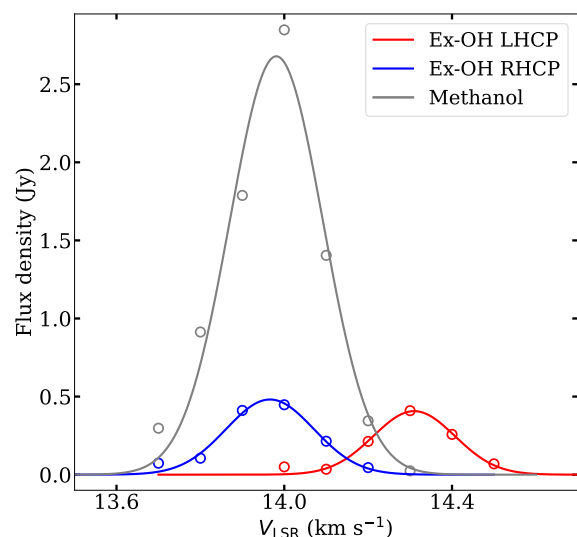


Fig. 1: Example of the overlap of both maser transitions when Zeeman splitting is identified in the ex-OH transition. Profiles are from a maser group in G43.149+0.013 named as  $Z_8$  in ex-OH (Table C.1). The dots correspond to the flux density measured on single-channel maps, and the lines are Gaussian profiles fit to the spectral features.

<sup>2</sup> <https://obs.vlba.nrao.edu/cst/>

Table 2: Rms noises ( $1\sigma$ ) in channels without emission for image cubes in each Stokes parameter.

Source name (1 b)	$\sigma_{\text{I\_meth}}$ (mJy beam $^{-1}$ )	$\sigma_{\text{I\_exOH}}$ (mJy beam $^{-1}$ )	$\sigma_{\text{Q\_exOH}}$ (mJy beam $^{-1}$ )	$\sigma_{\text{U\_exOH}}$ (mJy beam $^{-1}$ )	$\sigma_{\text{LHCP\_exOH}}$ (mJy beam $^{-1}$ )	$\sigma_{\text{RHCP\_exOH}}$ (mJy beam $^{-1}$ )
G20.237+0.065	18.4	17.0	16.6	17.6	19.4	22.8
G24.148-0.009	28.7	12.7	12.3	12.6	16.9	15.9
G25.648+1.049	15.9	12.0	11.5	11.8	18.2	16.4
G34.267-0.210	16.3	8.0	8.1	8.9	11.4	10.1
G43.149+0.013	14.3	15.2	16.5	16.0	22.3	20.6
G48.990-0.299	55.6	15.9	16.4	15.9	23.0	20.7
G49.490-0.388	59.8	19.9	21.7	22.1	29.8	27.1
G69.540-0.976	18.3	17.8	18.2	17.5	20.6	21.1
G81.871+0.781	8.5	9.9	9.8	10.2	14.9	13.9
G108.766-0.986	13.9	27.2	22.5	21.9	33.5	31.7

### 3. Results

The distributions of the Stokes  $I$  maser spots and spectra of methanol and ex-OH are presented in the top panels on Figs. 2, 3, and B.1-B.8. When the coincidence of both transitions occurs, we mark them with non-filled symbols. The kinematic distances used to estimate linear sizes of sources were calculated using the parallax-based distance calculator<sup>3</sup> by Reid et al. (2019). In some cases, the ambiguity was resolved using the H $\alpha$  absorption by Green & McClure-Griffiths (2011). In the case of G48.990-0.299, G69.540-0.976, and G81.871+0.781, direct distance measurements were available via the trigonometric parallax method.

The LHCP and RHCP ex-OH emission is presented in the middle panels of Figs. 2, 3, and B.1-B.8, where we also give the magnetic field strength along the line of sight derived from the identified Zeeman pairs. The relationship between Stokes  $I$  and both circular polarizations is:  $0.5 \times (\text{RHCP} + \text{LHCP})$ . As is noted in Sect. 2, we measured the properties of RHCP and LHCP spots in the same position as  $I$  spots in each channel to ensure that we sampled the same gas when identifying Zeeman pairs. Only position error  $\delta_2$  is applicable to comparisons within the same data cube. The worst accuracy for the faintest spots is  $\sim 16$  mas, which is less than the physical size of the emitting regions, estimated from the angular extent of series of spots in consecutive channels, ensuring that detected associations between the polarizations are genuine.

Table C.1 lists the parameters of the identified Zeeman pairs: the flux density of the brightest maser spot in each polarization ( $S_{\text{max}}$ ) and the parameters of the fit Gaussian profile to the spectrum; the peak amplitude ( $S_{\text{fit}}$ ), the full width at half maximum of the profile ( $FWHM_{\text{fit}}$ ), and the peak velocity ( $V_{\text{fit}}$ ). We also list  $\Delta V_Z = V_{\text{fit}}(\text{RHCP}) - V_{\text{fit}}(\text{LHCP})$ , with the errors based on the accuracy of the fit Gaussian profiles, and the de-magnetized velocity that is assumed to be the mean of velocities of both polarized peaks:  $V_d = 0.5 \times (V_{\text{fit}}(\text{RHCP}) + V_{\text{fit}}(\text{LHCP}))$ . Using the formula  $\Delta V_Z/B = 0.056$  from Baudry et al. (1997), we calculated the magnetic field along the line of sight ( $B_{\text{los}}$ ), which is included in Figs. 2, 3, and B.1-B.8. The field is directed away from us when  $V_{\text{fit}}(\text{RHCP}) > V_{\text{fit}}(\text{LHCP})$  and is directed toward us when  $V_{\text{fit}}(\text{RHCP}) < V_{\text{fit}}(\text{LHCP})$ .

The bottom panels in Figs. 2, 3, and B.1-B.8 show the circular and linear degrees of polarization of ex-OH emission. They were calculated as follows:  $m_c = V/I$  and  $m_l = P_1/I$ , respectively. The  $V$  Stokes parameter, which is defined as  $0.5 \times (\text{RHCP} - \text{LHCP})$ , and the linearly polarized flux density,  $P_1$ , which is defined as  $(Q^2 + U^2)^{0.5}$ , are also presented. All spots

with nonzero linearly polarized emission are summarized in Table C.2 with their values of  $I$ ,  $Q$ ,  $U$ ,  $P_1$ , and  $m_l$ , the electric vector PA (defined as  $\chi_1 = 0.5 \times \arctan(U/Q)$ , positive from north to east),  $m_c$ , and the total polarization  $m_f = \sqrt{m_l^2 + m_c^2}$ . The linear polarization vector is directed along the PA of the electric vector. The orientation of the magnetic field,  $\Phi_B$ , is perpendicular to the linear polarization vector for  $\sigma$  components. When the fraction of linear polarization exceeds 71%, the amplification of  $\pi$  component gain is high and so  $\Phi_B$  can become parallel (e.g., Fish & Reid 2006).

We calculated the brightness temperature ( $T_B$ ) as in Wrobel & Walker (1999), for the brightest maser in each source and transition. Since the maser spots are unresolved and we used the synthesized beam size as the area of the emission,  $T_B$  is a lower limit. Below, we describe the individual sources in detail.

#### G20.237+0.065 (hereafter G20)

The maser distributions of G20.237+0.065 are presented in Fig. 2. The calculated near-kinematic distance is  $4.41 \pm 0.39$  kpc; the kinematic distance ambiguity was resolved by Green & McClure-Griffiths (2011) through H $\alpha$  self-absorption. The methanol maser emission is spread over  $170 \text{ mas} \times 150 \text{ mas}$ , corresponding to  $750 \text{ au} \times 660 \text{ au}$ . The morphology is complex, as was noted by Bartkiewicz et al. (2016) based on EVN images. The ex-OH emission lies within a region of similar extent,  $150 \text{ mas} \times 150 \text{ mas}$  ( $660 \text{ au} \times 660 \text{ au}$ ), but this line is significantly weaker and has a simpler structure – two groups of spots in the northeast and one in the southwest. The 6.7 GHz transition covers a  $V_{\text{LSR}}$  range from  $67.7$  to  $77.5 \text{ km s}^{-1}$ , and the 6.035 GHz transition covers from  $71.1$  to  $77.0 \text{ km s}^{-1}$ . We notice that in the most redshifted group, in the southwest, the two transitions coincide in velocity (within  $0.5 \text{ km s}^{-1}$ ) and position (within  $34 \text{ mas}$ ) and can be assumed to be coexisting in the same volume of gas, as was analyzed according to the procedure described in Sect. 2:  $34 \text{ mas} \leq 0.5(42 \text{ mas} + 33 \text{ mas})$ . The brightness temperature ( $T_B$ ) is at least  $1.6 \times 10^9 \text{ K}$  for the methanol masers and  $9.9 \times 10^7 \text{ K}$  for the ex-OH masers.

We identify three Zeeman pairs ( $Z_1$ - $Z_3$ ) in the ex-OH line, which indicate magnetic field strengths from  $+0.2$  to  $-3.6 \text{ mG}$  (Table C.1). The magnetic field is directed toward the observer, with a possible reversal toward the middle group. The degree of circular polarization is below 40% for  $Z_1$  and  $Z_2$ ; for the redshifted pair ( $Z_3$ ), we detect 29-74% of circular polarization. We did not detect linear polarization from this source above a threshold of  $34 \text{ mJy}$  ( $3\sigma$ ), implying that the magnetic field lines may be oriented closer to the line of sight.

<sup>3</sup> <http://bessel.vlbi-astrometry.org/node/378>

Table 3: Parameters of the brightest methanol maser spot in each target.

Source name (l b)	RA $_{S_p^{6.7}} \pm \delta_{\text{tot,RA}}$ (h m s s)	Dec $_{S_p^{6.7}} \pm \delta_{\text{tot,Dec}}$ ( $^{\circ}$ ' " ")	$V_p^{6.7}$ (km s $^{-1}$ )	$S_p^{6.7}$ (Jy beam $^{-1}$ )	$T_B$ $\times 10^9$ (K)	$\gamma_{6.7}$ (mas)
G20.237+0.065	18 27 44.5613 $\pm$ 0.0029	-11 14 54.216 $\pm$ 0.043	72.0	22.65	1.58	41.8
G24.148-0.009	18 35 20.9399 $\pm$ 0.0014	-07 48 55.775 $\pm$ 0.021	17.6	15.32	1.12	19.0
G25.648+1.049	18 34 20.9069 $\pm$ 0.0032	-05 59 42.261 $\pm$ 0.048	41.8	95.01	6.77	47.1
G34.267-0.210	18 54 37.2500 $\pm$ 0.0029	01 05 33.615 $\pm$ 0.043	54.5	5.90	0.41	42.2
G43.149+0.013	19 10 11.0464 $\pm$ 0.0042	09 05 20.371 $\pm$ 0.063	13.2	7.51	0.59	62.3
G48.990-0.299	19 22 26.1312 $\pm$ 0.0014	14 06 39.696 $\pm$ 0.021	71.5	2.78	0.19	20.5
G49.490-0.388	19 23 43.9461 $\pm$ 0.0018	14 30 34.366 $\pm$ 0.027	59.2	613.87	41.44	25.8
G69.540-0.976	20 10 09.0436 $\pm$ 0.0025	31 31 34.989 $\pm$ 0.038	14.6	65.14	4.39	36.7
G81.871+0.781	20 38 36.4097 $\pm$ 0.0038	42 37 35.110 $\pm$ 0.056	4.6	195.65	14.32	53.0
G108.766-0.986	22 58 51.1857 $\pm$ 0.0018	58 45 14.380 $\pm$ 0.026	-45.7	12.25	0.83	25.4

**Notes.** Note that the  $\gamma$  parameter is estimated for the weakest methanol spot.

Table 4: The parameters of the brightest ex-OH maser spots (Stokes I) in each target.

Source name (l b)	RA $_{S_p^{6.035}} \pm \delta_{\text{tot,RA}}$ (h m s s)	Dec $_{S_p^{6.035}} \pm \delta_{\text{tot,Dec}}$ ( $^{\circ}$ ' " ")	$V_p^{6.035}$ (km s $^{-1}$ )	$S_p^{6.035}$ (Jy beam $^{-1}$ )	$T_B$ $\times 10^7$ (K)	$\gamma_{6.035}$ (mas)
G20.237-0.065	18 27 44.5623 $\pm$ 0.0023	-11 14 54.065 $\pm$ 0.034	71.4	1.29	9.89	32.6
G24.148-0.009	18 35 20.9398 $\pm$ 0.0025	-07 48 55.773 $\pm$ 0.037	17.2	1.14	8.68	35.8
G25.648+1.049	18 34 20.9313 $\pm$ 0.0034	-05 59 42.655 $\pm$ 0.051	39.5	1.55	12.72	49.7
G34.267-0.210	18 54 37.2497 $\pm$ 0.0030	01 05 33.622 $\pm$ 0.045	54.1	1.91	14.62	44.1
G43.149+0.013	19 10 11.0632 $\pm$ 0.0037	09 05 20.250 $\pm$ 0.056	11.1	1.44	10.24	54.4
G48.990-0.299	19 22 26.1350 $\pm$ 0.0019	14 06 39.704 $\pm$ 0.018	68.1	1.12	20.43	17.3
G49.490-0.388	19 23 43.9017 $\pm$ 0.0015	14 30 33.548 $\pm$ 0.023	54.8	5.32	40.14	22.1
G69.540-0.976	20 10 09.0859 $\pm$ 0.0023	31 31 34.840 $\pm$ 0.035	14.4	4.46	34.41	33.6
G81.871+0.781	20 38 36.4209 $\pm$ 0.0054	42 37 34.741 $\pm$ 0.081	6.7	2.72	20.67	79.1
G108.766-0.986	22 58 51.1786 $\pm$ 0.0021	58 45 14.317 $\pm$ 0.031	-45.9	0.83	6.27	30.2

**Notes.** Note that the  $\gamma$  parameter is estimated for the weakest ex-OH spot.

There is another 6.7 GHz masing region 8''6 toward the northeast, G20.239+0.065 (see Sect. 4.1). We recovered the methanol emission similarly as Bartkiewicz et al. (2016) but we have no detection of ex-OH maser above a threshold of 51 mJy beam $^{-1}$  ( $3\sigma$ ).

#### G24.148-0.009 (hereafter G24)

The maser emission from both transitions is presented in Fig. 3. The near kinematic distance is  $1.66 \pm 0.25$  kpc with a probability of 69%, corresponding to the central velocity<sup>4</sup> of  $18.1$  km s $^{-1}$ . The masing region is compact and elongated in the north-south direction. The centroids of the 6.7 GHz spots occur within an area of  $11 \text{ mas} \times 44 \text{ mas}$  ( $18 \text{ au} \times 73 \text{ au}$ ) and those of the ex-OH spots within an area of  $3 \text{ mas} \times 22 \text{ mas}$  ( $5 \text{ au} \times 37 \text{ au}$ ). The emission covers the velocity ranges from  $16.8$  km s $^{-1}$  to  $19.6$  km s $^{-1}$  at 6.7 GHz and from  $16.6$  km s $^{-1}$  to  $17.4$  km s $^{-1}$  at the 6.035 GHz line. Coexistence of both lines occurs in the whole masing region except for the redshifted emission of the methanol line. The  $T_B$  is at least  $1.1 \times 10^9$  K for methanol masers and  $8.7 \times 10^7$  K for ex-OH masers.

We are not able to identify Zeeman splitting due to a different number of spectral features in each polarization and attenuation or suppression of the LHCP feature, therefore estimation of the strength of the magnetic field is impossible. The source

<sup>4</sup> We use the central velocity of masers, in cases where we do not have measurements of systemic velocities.

is strongly polarized (bottom panel of Fig. 3);  $m_c$  is from 59% to 100%, and three out of nine spots show  $m_l$  within a range from 24% to 38%. The directions of linear polarization vectors are from  $-52^\circ$  to  $-70^\circ$  (Table C.2), indicating a magnetic field oriented nearly northeast-southwest at  $\Phi_B = +30 \pm 6^\circ$ .

#### G25.648+1.049 (hereafter G25)

The maser distribution is presented in Fig. B.1. The near kinematic distance is  $3.8 \pm 1$  kpc with a probability of 70% for the central velocity of  $41.4$  km s $^{-1}$ . Green & McClure-Griffiths (2011) obtains a far kinematic distance of  $12.5 \pm 0.4$  kpc, derived from H $\alpha$  self-absorption.

The regions of methanol and excited OH emission are clearly separated both in the spatial and in the velocity domain. Each transition forms three groups and ex-OH masers lie southward relative to the methanol masers. The 6.7 GHz maser covers an area of  $450 \text{ mas} \times 325 \text{ mas}$  ( $1700 \text{ au} \times 1225 \text{ au}$  and  $5600 \times 4100 \text{ au}$  for the near and far kinematic distances, respectively) and appears at a velocity range of  $38.3$ - $43.8$  km s $^{-1}$ , whereas the 6.035 GHz maser is spread over  $300 \text{ mas} \times 100 \text{ mas}$  ( $1130 \text{ au} \times 377 \text{ au}$  and  $3750 \times 1250 \text{ au}$  for the near and far kinematic distances, respectively) and covers a velocity range of  $38.3$ - $39.9$  km s $^{-1}$ . The smallest angular separation between these two transitions is  $\sim 50$  mas. The  $T_B$  is at least  $6.8 \times 10^9$  K for the methanol masers and  $1.3 \times 10^8$  K for the ex-OH masers.

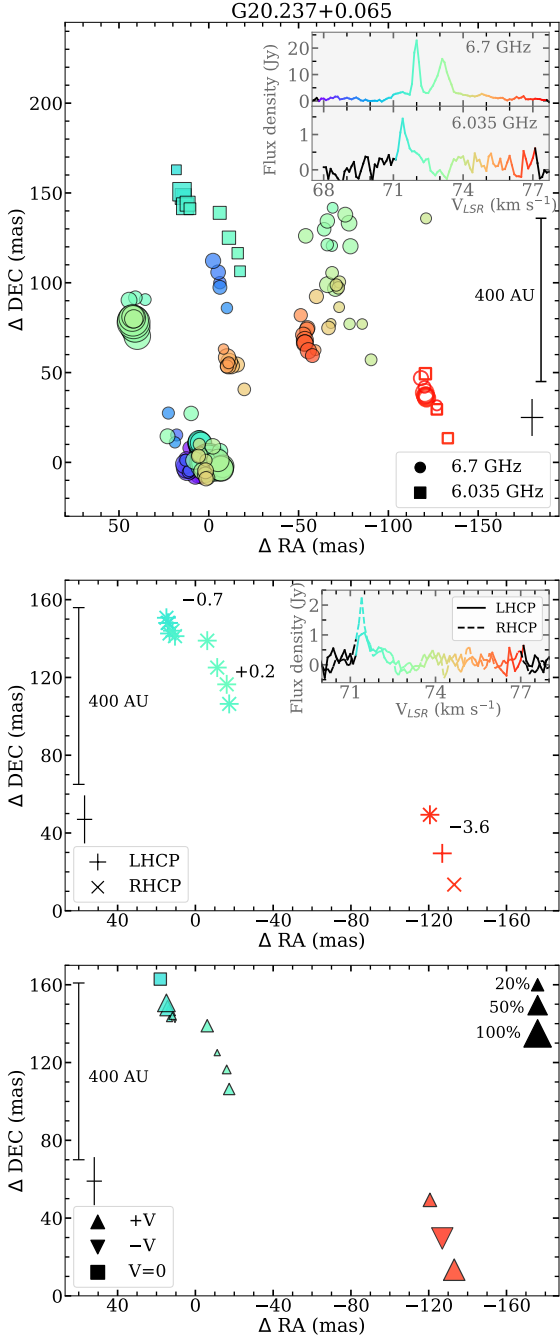


Fig. 2: Methanol and ex-OH maser emission in G20.237+0.065. **Top:** Distribution of the 6.7 (circles) and 6.035 GHz (squares) Stokes *I* maser spots. Symbol size is proportional to the square root of intensity, and the color corresponds to the LSR velocity, as is given in the total intensity spectra inserted at the top. LSR velocity ranges with no detections are shown in black. Non-filled symbols correspond to cases in which the coincidence of both transitions occurs. **Middle:** Distributions of LHCP and RHCP of ex-OH maser spots. Numbers are the values of the line-of-sight magnetic field strength (in milligauss). **Bottom:** Distribution of *V* Stokes of ex-OH. Symbol size is proportional to the degree of circular polarization. The black cross indicates the maximum position error for the spot.

Three Zeeman pairs are identified, showing a similar line-of-sight magnetic field strength from  $-6.2$  to  $-7.0$  mG and in-

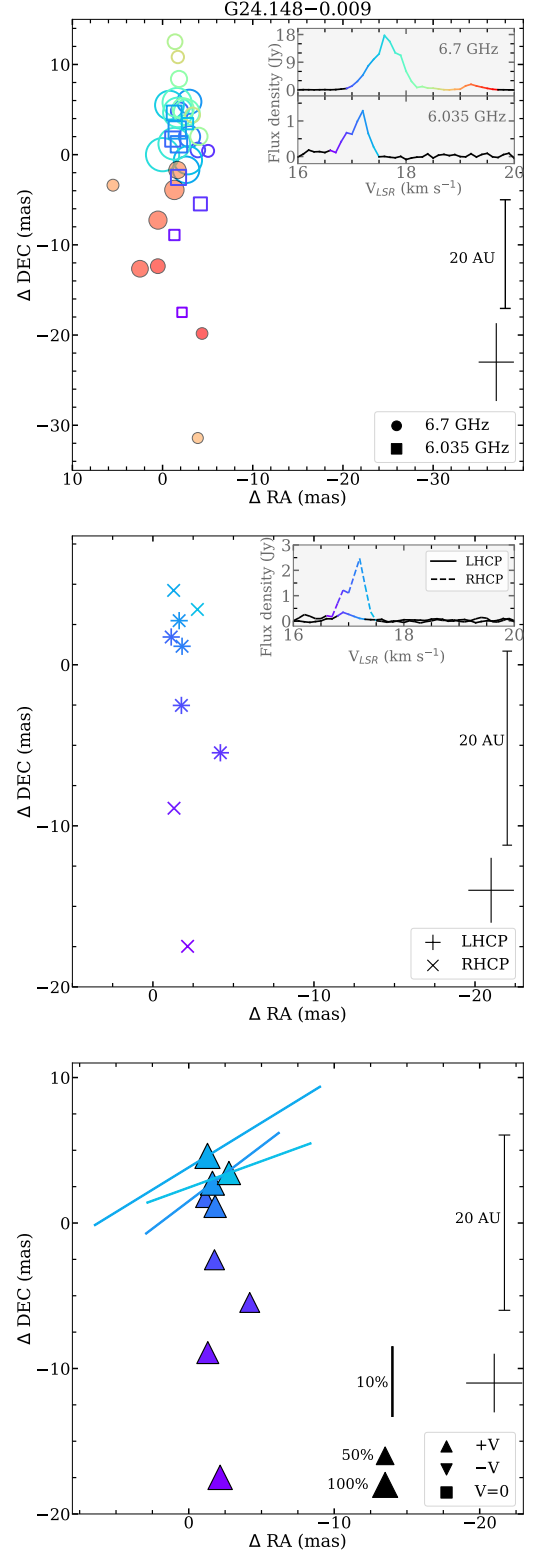


Fig. 3: Same as Fig. 2 but for G24.148-0.009. In the bottom panel, the bars represent the direction of the planes containing the electric field vector. Their lengths are proportional to the percentage of linear polarization and their colors correspond to the LSR velocity, as is indicated in the inserted spectra in the top and middle panels.

dicating that the magnetic field is directed toward the observer

(Table C.1). The emission shows strong circular polarization; 16 out of 31 spots are polarized above 80%, and seven spots have  $m_c$  below 50%. One spot has linear polarization with  $m_l=95\%$  and a PA of  $+5^\circ$  (Table C.2), indicating a magnetic field directed east-west with  $\Theta_B = -85 \pm 2^\circ$ . We did not find strong evidence for the existence of a  $\pi$  component (see Sect. 4.3.3), so we assume that the linear polarization comes from  $\sigma$  components and that  $\Theta_B$  is perpendicular to the linearly polarized vector.

#### G34.267–0.210 (hereafter G34)

The results are presented in Fig. B.2. The near and far kinematic distances are  $2.94 \pm 0.18$  kpc and  $9.6 \pm 0.5$  kpc, with similar probabilities (Reid et al. 2019). The methanol maser emission is significantly more complex compared with ex-OH. It is spread over an area of  $125 \text{ mas} \times 220 \text{ mas}$  ( $370 \text{ au} \times 650 \text{ au}$  and  $1200 \text{ au} \times 2100 \text{ au}$  for the near and far kinematic distances, respectively) and emission occurs in the LSR velocity range from  $47.8$  to  $54.9 \text{ km s}^{-1}$ . The redshifted part is located in the east and coincides with the ex-OH maser spots within  $40 \text{ mas}$  and  $0.1 \text{ km s}^{-1}$ . The  $T_B$  is at least  $4.1 \times 10^8 \text{ K}$  for the methanol masers and  $1.5 \times 10^8 \text{ K}$  for the ex-OH masers.

We are not able to identify any Zeeman pairs in the ex-OH transition. The LHCP emission is brighter but RHCP shows a more complicated spectrum. We notice a clear shift in velocity between these two polarizations, with RHCP being more positive; that indicates that the  $B_{\text{los}}$  is directed away from the observer and puts a lower limit on the magnetic field strength of  $2.84 \text{ mG}$ . Six out of eleven spots have  $m_c$  above 80%, and seven spots show  $m_l$  from 6% to 36%. The planes of electric vectors rotate from one masing group to another over  $50 \text{ au}$  without any systematic changes.  $\Phi_B$  for the brightest four spots is  $-58 \pm 21^\circ$ , while for three weaker it is  $+23 \pm 3^\circ$ . Therefore, we cannot clearly state the direction of the magnetic field in this target.

#### G43.149+0.013 (hereafter G43)

The ex-OH and methanol maser emission is presented in Fig. B.3. This target is part of the high-mass star formation region W49N lying at a distance of  $11.11^{+0.79}_{-0.69}$  kpc (Zhang et al. 2013). In this source, the ex-OH masers are more complex than the methanol masers. The ex-OH emission is spread over  $280 \text{ mas} \times 250 \text{ mas}$  ( $3100 \text{ au} \times 2800 \text{ au}$ ) and over a LSR velocity range of  $9.5$ – $14.5 \text{ km s}^{-1}$ . It forms two groups elongated perpendicular to each other (the blueshifted emission is at a PA, from north to east, of  $+77^\circ$ , while the redshifted emission is at  $-53^\circ$ ). The methanol masers appear at redshifted velocities from  $13 \text{ km s}^{-1}$  to  $14.2 \text{ km s}^{-1}$ , in three groups, similar to the appearance in VLBI images (Bartkiewicz et al. 2014), over a region of  $150 \text{ mas} \times 110 \text{ mas}$  ( $1700 \text{ au} \times 1200 \text{ au}$ ). We notice the coincidence of both maser transitions in these three groups. The brightest, blueshifted part of the ex-OH transition appears not to have methanol maser counterparts. The  $T_B$  is at least  $5.9 \times 10^8 \text{ K}$  for the methanol masers and  $1.0 \times 10^8 \text{ K}$  for the ex-OH masers.

We identify eight Zeeman pairs. The two most easterly ones imply values of the magnetic field strength above  $+3.0 \text{ mG}$  directed away from the observer, while in the remaining clumps the field is directed toward the observer with values from  $-1.3$  to  $-6.5 \text{ mG}$ . That indicates the reversal of the magnetic field. Twenty out of fifty-four spots are circularly polarized above 80% and twenty-two spots below 50%. Eight spots (all belonging to three Zeeman pairs) show linear polarization, from 8% to 48%. The mean  $\Phi_B$  of the eastern part is  $-66 \pm 24^\circ$ , while the elec-

tric vector of the redshifted linearly polarized ex-OH spot is  $15^\circ$ , indicating that  $\Phi_B = -75 \pm 9^\circ$ . Such differences in the spot distributions and the orientation of the magnetic field may indicate that these two regions are related to diverse kinematic regions.

#### G48.990–0.299 (hereafter G48)

The results are presented in Fig. B.4. The distance is  $5.62^{+0.59}_{-0.49}$  kpc, as was estimated by Nagayama et al. (2015). Again, in this target, the ex-OH emission is more complex than the methanol masers. The methanol maser emission shows a simple structure, two spots at LSR velocities of  $71.5 \text{ km s}^{-1}$  and  $71.6 \text{ km s}^{-1}$ . The ex-OH masers appear in a wider velocity range from  $66.7$  to  $69.6 \text{ km s}^{-1}$  and cover a region of  $290 \text{ mas} \times 135 \text{ mas}$ , which corresponds to  $1630 \text{ au} \times 760 \text{ au}$ . They are elongated along a line from southeast to northwest. The  $T_B$  is at least  $1.9 \times 10^8 \text{ K}$  for the methanol masers and  $2.0 \times 10^8 \text{ K}$  for the ex-OH masers. Nagayama et al. (2015) report water maser emission at  $22 \text{ GHz}$  at LSR velocities from  $65 \text{ km s}^{-1}$  to  $68 \text{ km s}^{-1}$  showing north-south elongation and proper motions implying expansion.

The ex-OH transition forms four Zeeman pairs. Two western groups have positive values of  $B_{\text{los}}$  ( $+2.7$  and  $+2.3 \text{ mG}$ ), directed away from the observer, and two eastern groups, separated by  $\sim 250 \text{ mas}$ , have negative values ( $-0.7$  and  $-4.8 \text{ mG}$ ) of  $B_{\text{los}}$ , indicating a magnetic field directed toward the observer. Circular polarization is below 50% for 18 out of 29 spots and above 80% for 5 out of 29 spots. Linear polarization is detected for six spots in the two brightest groups, with degrees 8–31%. The electric vectors are consistent over the whole region with PAs from  $-17$  to  $-56^\circ$ , indicating  $\Phi_B = +54 \pm 7^\circ$ . Again, we see a clear reversal of the line-of-sight magnetic field.

#### G49.490–0.388 (hereafter G49)

This target belongs to the well-known high-mass star formation region W51. The ex-OH and methanol maser emission is presented in Fig. B.5. The distance is  $5.41^{+0.31}_{-0.28}$  kpc, based on the trigonometric parallax measurement using water masers by Sato et al. (2010); we note that the result of  $5.1^{+2.9}_{-1.4}$  kpc using  $12.2 \text{ GHz}$  methanol masers, by Xu et al. (2009), is less accurate. The  $6.7 \text{ GHz}$  methanol maser emission covers an area of  $0':47 \times 0':55$ , corresponding to  $2550 \text{ au} \times 3000 \text{ au}$ , and appears in two velocity ranges, from  $51.2$  to  $52.3 \text{ km s}^{-1}$  and from  $57.5$  to  $60.2 \text{ km s}^{-1}$ . The emission is very bright, with a maximum flux density of  $684 \text{ Jy}$ . The morphology agrees well with the distribution derived from EVN observations, but it is more extended. Fujisawa et al. (2014) reported a smaller masing region of  $0':37 \times 0':31$ . However, Etoka et al. (2012) imaged emission over  $3'' \times 2''$ . Ex-OH masers are weaker with a maximum flux density of  $7 \text{ Jy}$  and are located in the west over a region of  $0':27 \times 0':53$  ( $1460 \text{ au} \times 2870 \text{ au}$ ) at intermediate LSR velocities from  $51.6$  to  $58.3 \text{ km s}^{-1}$ . Like Etoka et al. (2012), we do not find any spatial overlap between the two transitions. The  $T_B$  is at least  $5.9 \times 10^8 \text{ K}$  for the methanol masers and  $1.0 \times 10^8 \text{ K}$  for the ex-OH masers.

We identified nine Zeeman pairs.  $Z_1$ – $Z_3$  are new ones compared with the results of Etoka et al. (2012) (their Table 3). For all groups, the field is directed away from the observer, and its values are from  $+3.3 \text{ mG}$  to  $+8.1 \text{ mG}$ , which is consistent with Etoka et al. (2012). The emission is strongly polarized; 41 of 85 spots have a degree of circular polarization above 80% and only 20 spots below 50%. Twenty spots in four Zeeman pairs

show linear polarization in the range 5–22%. The mean PA of the electric vectors of  $0\pm 10^\circ$  indicates the magnetic field oriented at  $-90^\circ$ . However, we notice different values of  $\chi_1$  for each maser group, similar to in G34.

#### G69.540–0.976 (hereafter G69)

This target is associated with the high-mass star formation region Onsala 1 (ON1). The maser distributions are presented in Fig. B.6. The distance based on the trigonometric parallax is  $2.57^{+0.34}_{-0.27}$  kpc (Rygl et al. 2010). The methanol masers cover an area of  $0''.47\times 1''.09$ , or  $1220\text{ au}\times 2800\text{ au}$ , over two ranges of LSR velocities, from  $-0.5\text{ km s}^{-1}$  to  $2.6\text{ km s}^{-1}$  and from  $14.1\text{ km s}^{-1}$  to  $15.7\text{ km s}^{-1}$ . The observed spatial distribution of the 6.7 GHz masers is more complex compared to images obtained using EVN in 2006–2008 by Rygl et al. (2010), since these authors reported only two groups with an angular separation of  $0''.94$ . However, our results agree well with the EVN images taken in 2015 by Surcis et al. (2022), in which three groups were reported similarly as by Sugiyama et al. (2011) using JVN in 2006–2008. The ex-OH masers are spread over  $1''.05\times 1''.08$ , i.e.  $2690\text{ au}\times 2775\text{ au}$ , and also come from two velocity ranges: from  $-1.6\text{ km s}^{-1}$  to  $2.3\text{ km s}^{-1}$  and from  $12.2\text{ km s}^{-1}$  to  $15.2\text{ km s}^{-1}$ . We identify two regions where the overlap of both transitions is seen: in the north, the blueshifted masers coincide within 46 mas (33.8 mas in RA and 31.6 mas in Dec); and in the south, the redshifted masers coincide within 28 mas (23.6 mas in RA and 13.6 mas in Dec). The  $T_B$  is at least  $4.4\times 10^9\text{ K}$  for the methanol masers and  $3.4\times 10^8\text{ K}$  for the ex-OH masers.

We identify five Zeeman pairs in the ex-OH transition, at redshifted velocities, implying a negative magnetic field (directed toward us):  $B_{\text{los}}$  is from  $-1.2\text{ mG}$  to  $-6.2\text{ mG}$ . The same five pairs were reported by Green et al. (2007). We are not able to identify the Zeeman splitting for the blueshifted emission due to different LCHP and RCHP spectral features. The degree of circular polarization is below 50% for 59 of 96 spots and above 80% for 38 spots. In each Zeeman pair, there are spots (in total 26) that are linearly polarized with degrees from 8% to 48%. The means of  $\Phi_B$  are:  $-50\pm 17^\circ$  for the northern and blueshifted region and  $+80\pm 12^\circ$  for the southern and redshifted region. Green et al. (2007) reported two ex-OH features with  $m_1$  of 18.5% and 10% and  $\chi_1$  of  $-87.7^\circ\pm 2^\circ$  and  $-42.5^\circ\pm 0.7^\circ$ , respectively. They correspond to the spots at the LSR velocity of  $14.3\text{--}14.5\text{ km s}^{-1}$  listed in Table C.2. We note that Surcis et al. (2022) estimated a mean magnetic field direction of  $-51\pm 69^\circ$  from linearly polarized methanol masers.

#### G81.871+0.781 (hereafter G81)

This target is in the well-known high-mass star formation region W75N. Its distance is  $1.30\pm 0.07\text{ kpc}$  (Rygl et al. 2012). The methanol and ex-OH maser distributions are presented in Fig. B.7. The methanol masers are spread over an area of  $0''.49\times 1''.065$ , or  $638\text{ au}\times 1384\text{ au}$ , and appear in the  $V_{\text{LSR}}$  range of  $2.6\text{--}9.7\text{ km s}^{-1}$ . That is consistent with EVN results from Rygl et al. (2012). Ex-OH maser emission is less complex; it is located in the central part of the 6.7 GHz emission over an area of  $59\text{ mas}\times 312\text{ mas}$  ( $77\text{ au}\times 406\text{ au}$ ), over a  $V_{\text{LSR}}$  range of  $6.2\text{--}9.2\text{ km s}^{-1}$ . It appears as three groups. We notice an overlap between the two masers in the southern group: two spots coincide within 21 mas (15.3 mas in RA and 14.7 mas in Dec). Similarly, in the northern group, six spots coincide within 65 mas (22 mas in RA and 61.6 mas in Dec), and in the centrally located group,

nine spots coincide within 61 mas (33.7 mas in RA and 50.5 mas in Dec). The  $T_B$  is at least  $14.3\times 10^9\text{ K}$  for the methanol masers and  $2.1\times 10^8\text{ K}$  for the ex-OH masers.

We report three Zeeman pairs, for which the  $B_{\text{los}}$  is positive and directed away from the observer with values of  $+2.3\text{ mG}$  for the southern group and of  $+7.3$  and  $+8.5\text{ mG}$  for the central pairs. In the northern group, we are not able to identify LHCP and RHCP features belonging to a likely Zeeman pair. The degree of circular polarization is above 80% for 16 of 39 spots and below 50% for 14 spots. Fourteen spots show linear polarization, the majority of which have a degree from 4% to 15%. Three redshifted spots at  $V_{\text{LSR}}$   $8.3\text{--}8.6\text{ km s}^{-1}$  are much more polarized; their degrees are 38–58%. The mean value of the PAs of the electric vector planes is  $29\pm 13^\circ$ , indicating a magnetic field directed approximately along  $-61^\circ$ . Again, the source shows diverse directions of the magnetic field, possibly reflecting changes in the gas kinematics.

#### G108.766–0.986 (hereafter G108)

The distributions of both methanol and ex-OH masers are compact ( $8\text{ mas}\times 11\text{ mas}$  and  $7\text{ mas}\times 30\text{ mas}$ , respectively) and well separated in position (by around 80 mas). These are presented in Fig. B.8. The near kinematic distance is  $2.81\pm 0.23\text{ kpc}$ , with a probability of 72% for the central velocity of  $-45.6\text{ km s}^{-1}$ , implying a spatial separation between the two maser transitions of 225 au. Both lines appear at a similar LSR velocity range, from  $-46.4\text{ km s}^{-1}$  to  $-44.8\text{ km s}^{-1}$  for the methanol maser and from  $-46.1\text{ km s}^{-1}$  to  $-44.8\text{ km s}^{-1}$  for the ex-OH maser line. The smallest angular separation between the two masers is 67 mas, which exceeds twice the  $\gamma$  parameter, and we assume no overlap of both transitions. The  $T_B$  is at least  $8.3\times 10^8\text{ K}$  for the methanol masers and  $6.3\times 10^7\text{ K}$  for the ex-OH masers.

We identify two Zeeman pairs and we estimate the value of the magnetic field as  $-8.5\text{ mG}$  and  $-10.5\text{ mG}$ , indicating that the  $B_{\text{los}}$  is directed toward the observer. The ex-OH emission consists of 12 spots, of which three are more than 80% circularly polarized and two are less than 50% polarized. Only one spot shows linear polarization with a degree of 12%, indicating the value of  $\Theta_B = +22\pm 9^\circ$ .

## 4. Discussion

### 4.1. Counterparts

First, we discuss the counterparts of HMYSOs at other frequencies to derive information on the HMYSO environment on a larger scale. Centimeter radio emission identifies thermal jet or UCHII regions and, thus, a more evolved stage of the HMYSO. The earliest phases are seen in the ALMA dust continuum emission at 1 and 3 mm, which identifies star-forming cores, disks, and envelopes. To trace outflows, and in particular the outflow direction, which is interesting to compare to the magnetic field orientation, we used 22 GHz water masers and archival ALMA<sup>5</sup> spectral line data of SiO, SO, and the CO isotopologs in ALMA Band 6. The SiO, SO, and water masers are all shock tracers, while the CO isotopologs ( $^{12}\text{CO}$ ,  $^{13}\text{CO}$ ) trace large-scale gas motions. We typically used  $^{13}\text{CO}$  because it is more widespread and brighter than the (often) optically thin  $\text{C}^{18}\text{O}$  transition but not as optically thick (and complex) as the  $^{12}\text{CO}$  line. For warm gas,  $\text{CH}_3\text{CN}$  and  $\text{HC}_3\text{N}$  can be used as disk tracers, and the

<sup>5</sup> The ALMA Science Archive is available at [https://almascience.org/aq/?result\\_view=observations](https://almascience.org/aq/?result_view=observations)

CH<sub>3</sub>CN *K* ladder to obtain rotational temperatures and H<sub>2</sub>CO along with thermal methanol to trace young star-forming object (YSO)-heated gas. To constrain the clump properties, we used *Spitzer* 3.5, 4.5, 6, 8, and 24  $\mu\text{m}$ , and *Herschel* 70  $\mu\text{m}$  data that trace the warm dust heated by the central object(s). In Table C.3, we list the HMYSOs' positions from the Hi-GAL catalog (Molinari et al. 2016a,b; Elia et al. 2021). The *Herschel* astrometric accuracy is  $\sim 2$  arcsec (Molinari et al. 2016a). The target positional accuracy of *Spitzer* is about 1 arcsec, and the angular resolution is  $\sim 2$  arcsec<sup>6</sup>. The detailed descriptions of counterparts of all sources along with figures are in Appendix D.

#### 4.2. Evolutionary stage

As a tracer of warm dust, the far IR 70  $\mu\text{m}$  emission increases in strength as the protostar evolves. Table C.3 shows the strongest 70  $\mu\text{m}$  emission for G49 and for G43, G25, and G48. That suggests that those objects are the most evolved in our sample. G20, G24, and G34 show weak 70  $\mu\text{m}$  emission, indicating an earlier evolutionary phase, but the ratio  $S_{70\mu\text{m}}/S_{24\mu\text{m}}$  suggests that only G34 is an early HMYSO. We do not have information about 70  $\mu\text{m}$  emission for G69, G81, and G108. Another evolutionary indicator is  $\frac{L_{\text{bol}}}{M}$  (Molinari et al. 2008). Higher values indicate a later evolutionary phase. This criterion also supported G43 as the most evolved source, followed by G25; these sources are also characterized by the highest average dust temperatures in our sample, of 39 and 40 K, respectively. Based on the  $\frac{L_{\text{bol}}}{M}$  indicator, G20 and G34 are the youngest sources, and G24 and G48 are slightly more evolved. All those sources have  $T_D$  in the range between 21 and 25 K. We do not have information about  $\frac{L_{\text{bol}}}{M}$  and  $T_D$  for G49, G69, G81, and G108. Both indicators, IR 70  $\mu\text{m}$  emission as well as  $\frac{L_{\text{bol}}}{M}$ , concern the evolutionary states of clumps, but these can host more than one core or YSO. A better evolutionary indicator for a single YSO is the existence of thermal jets or a UCH<sub>II</sub> region. The sources with the strongest UCH<sub>II</sub> emission are G69, G43, and G48. In the case of G20 and G24, we did not find any confirmation as to whether observable radio continuum emission is related to a UCH<sub>II</sub> region or to a jet. However, the  $S_{70\mu\text{m}}/S_{24\mu\text{m}}$  ratio indicates that both sources are in late evolutionary phases, so we can assume that the radio continuum emission is related to UCH<sub>II</sub> emission, rather than to a thermal jet. G81 is associated with the radio continuum VLA1, which was identified as a radio jet. Also, G25 shows evidence that the radio continuum is associated with the radio jet. G34 and G108 do not have observable radio continuum emission. G49 is close to the UCH<sub>II</sub> but the maser emission can be related to the eastern core, which is the dominant accretion source in that region (Shi et al. 2010) and where the radio continuum was not detected (Gaume et al. 1993). We further analyze the source evolutionary phase in Sect. 4.4.

#### 4.3. Polarization properties and magnetic field

##### 4.3.1. Zeeman pairs

In total, we have identified 37 Zeeman pairs in eight HMYSOs: G20, G25, G43, G48, G49, G69, G81, and G108. We list the observed and fit peak flux densities and other parameters for all Zeeman pairs in Table C.1. Toward G24, we are not able to identify any Zeeman splitting due to the weakness of LHCP emission, and similarly, toward G34, we do not report any Zeeman splitting since it is impossible to define clearly the RHCP fea-

ture related to the single LHCP feature appearing in the ex-OH emission. The calculated magnetic field along the line of sight is from 0.2 mG up to 10.6 mG, with mean and median values of 4.8 mG and 5.2 mG, respectively. These values are typical for high-mass star-forming regions (e.g., Bartkiewicz et al. 2005, Fish et al. 2005, Vlemmings 2008, Green et al. 2015). However, Surcis et al. (2022) report slightly higher  $|B_{\text{los}}|$ , in a range from 9 mG to 40 mG in their sample of 31 targets, based on methanol masers' 6.7 GHz transition.

The direction of  $B_{\text{los}}$  is consistent for all measurements for five sources. The magnetic field is directed toward the observer in G25, G69, and G108 and away from the observer in G49 and G81. In the case of G43 and G48, we observe magnetic field reversals similar to the one reported for Cep A (Bartkiewicz et al. 2005). This may indicate a toroidal component of the magnetic field related to a disk. We do not notice any dependence between the size of the masing region and the magnetic field reversals. G43 and G48 are sampled by the Zeeman pairs over regions of 2000-3600 au, similar to G69, which shows the magnetic field directed to the observer over the whole region.

The relationship between the strength of the magnetic field and gas number density in molecular clouds in which the contraction is driven by ambipolar diffusion is defined as  $|B| \sim n^{0.47}$  (Crutcher 1999). We estimated the gas density following Bayandina et al. (2014), considering  $B_{\text{los}}$  in the range of 0.2-10.6 mG, which leads to derived gas densities ( $n_{\text{H}_2}$ ) in the range from 0.1 to  $378 \times 10^6 \text{ cm}^{-3}$ .

##### 4.3.2. Sky-plane B orientation

In nine HMYSOs, we found linearly polarized ex-OH masers: G24, G25, G34, G43, G48, G49, G69, G81, and G108. The linear polarization percentage is generally low, less than 40% for the majority of spots, and the mean and median are 20% and 15%, respectively (Fig. 4). G49 and G69 show the most numerous linearly polarized spots (more than 20). In two sources, G25 and G108, we found only one maser spot with  $m_l$  of 95% and 12%, respectively. In G25, a linearly polarized ex-OH maser spot indicates that the plane of the magnetic field is  $-85 \pm 2^\circ$  if the emission is associated with a  $\sigma$  component or  $+5 \pm 2^\circ$  if the emission is associated with a  $\pi$  component. In both cases, the magnetic field is not parallel or perpendicular to the outflow.

In G20, we did not find any linearly polarized emission above a threshold of  $2\sigma$ , implying that the magnetic field lines may be oriented closer to the line of sight. In G24 and G48, the electric vectors are well ordered, as are the vectors for the most blueshifted emission from G43. That indicates a consistent large-scale magnetic field orientation in the sky plane. Similar well-ordered linear polarized vectors were noticed by Surcis et al. (2013, 2015, 2019, 2022) from observations of bright 6.7 GHz methanol masers.

In G34, G49, G69, and G81, and the more redshifted parts of G43, the directions of electric vectors are strongly variable, and changes do not correlate with spot velocities. Koch et al. (2018) used ALMA dust polarization observations to estimate the direction of the magnetic field at different angular scales in G49 (W51e2e): at a resolution of 2 arcsec, the magnetic field is directed almost east to west, while at the higher angular resolution it is radially distributed, suggesting that the field is being dragged by the mass inflow. Ex-OH masers, lying offset from the young star and indicating a mean magnetic field oriented from east to west, fit well into this picture by tracking the large-scale magnetic field. Etoka et al. (2012) inferred that the ex-OH was part of a flow in which the dynamics were magnetically dominated.

<sup>6</sup> <https://irsa.ipac.caltech.edu/>

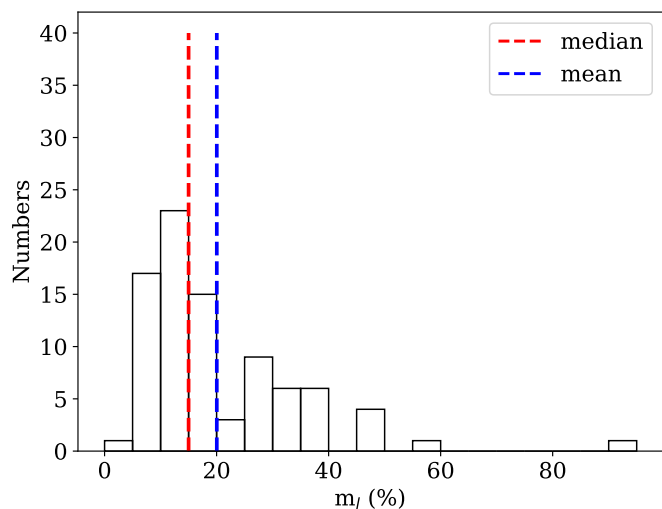


Fig. 4: Histogram of the percentage of linear polarization of all spots with detected linearly polarized emission. They are listed in Table C.2.

The magnetic field in G81, estimated from 18 cm OH masers by Hutawarakorn et al. (2002), reverses its direction on opposite sides of the disk, indicating a toroidal component of the magnetic field in the disk. Surcis et al. (2011) analysed the 22 GHz water masers associated with the VLA 1 and VLA 2 radio continuum sources. They reported a tightly ordered magnetic field around VLA 1 (aligned with the large-scale molecular outflow) and revealed an ordered magnetic field around VLA 2 (not parallel to the outflow). These strong magnetic fields, 0.7 G and 1.7 G, around VLA 1 and VLA 2, respectively, are related to shock compression of the gas. It is not easy to compare our results with the previous observations due to the time difference and proper motions of masers, which might be significant at this relatively close distance. We do not detect such a magnetic field reversal, since the ex-OH masers trace a more compact region than the 18 cm OH masers (2 arcsec). The magnetic field strength and orientation (away from the observer) derived from Zeeman splitting of ex-OH is consistent with measurements of the Zeeman splitting of 18 cm OH (see Fig. 11 of Hutawarakorn et al. 2002).

Table 5 lists the mean directions of the magnetic fields estimated using linearly polarized ex-OH masers ( $\Phi_B$ ), methanol and ex-OH elongation directions ( $PA_{6.7}$  and  $PA_{6.035}$ ), estimated from least-square fitting to the spot distributions. These are compared with the directions of outflows ( $PA_{out}$ ) where available (see Sect. 4.1). Based on the Kolmogorov-Smirnov test, we cannot find any correlation for the linear distributions of both masers with the outflows and with the estimated magnetic field orientations in the sky plane as well as between outflows and magnetic field vectors themselves. Even for the targets with the most elongated maser structures, such as G24, G43, G48, or G81, we still cannot sketch a clear scenario relating to maser structures and the magnetic field. This is similar to the conclusions of Surcis et al. (2013). However, in Surcis et al. (2022), the summary for a whole sample of 31 targets reports a bimodal distribution, with: 1) half the magnetic field directions being perpendicular, and 2) the other half being parallel to the outflow. It is difficult to study dependencies between sub-arcsecond maser data and images with a larger angular scale searching for outflows and disks.

#### 4.3.3. Zeeman triplets

Green et al. (2015) found 18 Zeeman triplet candidates among 112 Zeeman patterns in the ex-OH transition (detection rate of 16%) when using ATCA with a spectral resolution of  $24 \text{ m s}^{-1}$ . As we reported above, we detected 37 Zeeman pairs. The circularly polarized features (RHCP and LHCP) are the  $\sigma$  components of the Zeeman splittings; they are shifted in the velocities by the magnetic field. A third component, the  $\pi$  component, is the linearly polarized feature, unshifted in velocity. When comparing the Zeeman pairs and the linearly polarized spots that we identified (Tables C.1 and C.2), we find that in eight cases (21%), namely  $Z_3$  and  $Z_4$  of G48,  $Z_6$  and  $Z_7$  of G49,  $Z_1$ ,  $Z_2$ , and  $Z_5$  of G69, and  $Z_2$  of G81, we can suspect the existence of a Zeeman triplet; we mark these candidates with “T” in Table C.2. However, better angular and spectral resolution is needed to confirm that.

In G25, the linearly polarized emission at the LSR velocity of  $39.6 \text{ km s}^{-1}$  differs by only one spectral channel ( $0.1 \text{ km s}^{-1}$ ) from the demagnetized velocity of  $39.506 \text{ km s}^{-1}$ . A similar ambiguity is in  $Z_1$  of G81. We mark such cases with “v” (for verification needed) in Table C.2, and again, observations with better angular and spectral resolution and good sensitivity are needed to verify the existence of Zeeman triplets.

In G43, the linearly polarized spots coincide with the RHCP feature of  $Z_2$ , LHCP of  $Z_8$ , and interestingly with both circularly polarized features of  $Z_3$  with an avoidance of the central velocities. Similarly, the avoidance of unshifted velocities is seen in G49 and  $Z_4$ ,  $Z_5$ . That can indicate that this emission is associated with the  $\sigma$  components, but also that the line-of-sight velocity can change due to effects such as turbulence.

Green et al. (2015) showed that the flux densities of the  $\pi$  components of the triplets are from 3% to 85% of the average circular component flux, with a median of 16%, indicating the detection of  $\pi$  components only toward the brightest Zeeman splittings. We do not confirm such a trend among our candidates for triplets. However, as we noted above, more sensitive and better angular and spectral resolution observations are needed to verify the existence of the potential Zeeman triplets. The lack of  $\pi$  components may be related to the magnetic field orientation; if the magnetic field is parallel to the line of sight, the  $\pi$  component is not seen.

#### 4.4. Coincidence and avoidance of ex-OH and methanol masers

We note that the 6.7 GHz methanol maser emission is brighter than the ex-OH line in all targets, but the ratio  $S_p^{6.7}/S_p^{6.035}$  is diverse, from 2.5 to 115 with a median of 15. In six of the targets, the 6.7 GHz methanol maser is spread over larger regions in the sky than the ex-OH maser, again with a broad range of size ratios, from 1.1 to 2700, with a median of 6. In G43, G48, and G69, the ex-OH line emission has more complex structures and covers larger regions than methanol masers and in G108 the size of both transitions is similar. It is possible that the behavior stems from a lower kinetic temperature. The estimates of  $T_{tot}$  from  $\text{CH}_3\text{CN}$  lines give much lower temperatures for G43 and G69 than for G20 and G25, where methanol masers are more complex (see Appendix A).

We carefully examined the data, searching for coexistence, according to our method described in the last paragraph of Sect. 2, of both maser lines. In six targets, namely G20, G24, G34, G43, G69, and G81, we find coincidences of both transitions, considering the astrometric positions and overlap of the

Table 5: Comparisons of positions angles of the magnetic field, methanol maser distributions, ex-OH distributions, and the PAs of outflows.

Source	$\Phi_B$ ( $^\circ$ )	$PA_{6.7}$ ( $^\circ$ )	$PA_{6.035}$ ( $^\circ$ )	$PA_{out}$ ( $^\circ$ )	$ PA_{6.7}-PA_{6.035} $ ( $^\circ$ )	$ \Phi_B-PA_{out} $ ( $^\circ$ )	$ \Phi_B-PA_{6.7} $ ( $^\circ$ )	$ \Phi_B-PA_{6.035} $ ( $^\circ$ )
G20.237	-	-70	+50	-	60	-	-	-
G24.148	+30±6	-1	+2	+90	3	60	21	28
G25.648	-85±2	-72	+84	-30	24	55	13	11
G34.267	+80±23	+8	+24	-	16	-	72	56
G43.149	-66±24/-75±9*	-/-54	+77/-53*	+40	-/1	106/115	-/21	37/22
G48.990	+54±7	+44	-69	+20 <sup>(1)</sup>	67	30	10	57
G49.490	-90±10	+41	+10	-46 <sup>(2)</sup>	31	44	49	80
G69.540	-50±17/+80±12**	+39/-68**	+47/-60**	-69 <sup>(3)</sup>	8/8	19/31	89/32	83/40
G81.871	-61±13	-4	-7	+43 <sup>(4)</sup>	3	76	57	54
G108.766	+22±9	-68	+4	-	72	-	90	18

**Notes.** Less reliable values are marked by italics: methanol maser emission in G48 consists of only two spots; therefore, the determined PA is not precise. \*Ex-OH masers in G43 form two diverse regions: eastern (blueshifted) and northwestern (redshifted), respectively. \*\*Ex-OH and methanol masers in G69 form two regions: northern blueshifted and southern redshifted emission.  $PA_{out}$  is estimated based on <sup>(1)</sup>Nagayama et al. (2015), <sup>(2)</sup>Goddi et al. (2020), <sup>(3)</sup>Kumar et al. (2004), <sup>(4)</sup>Torrelles et al. (1997).

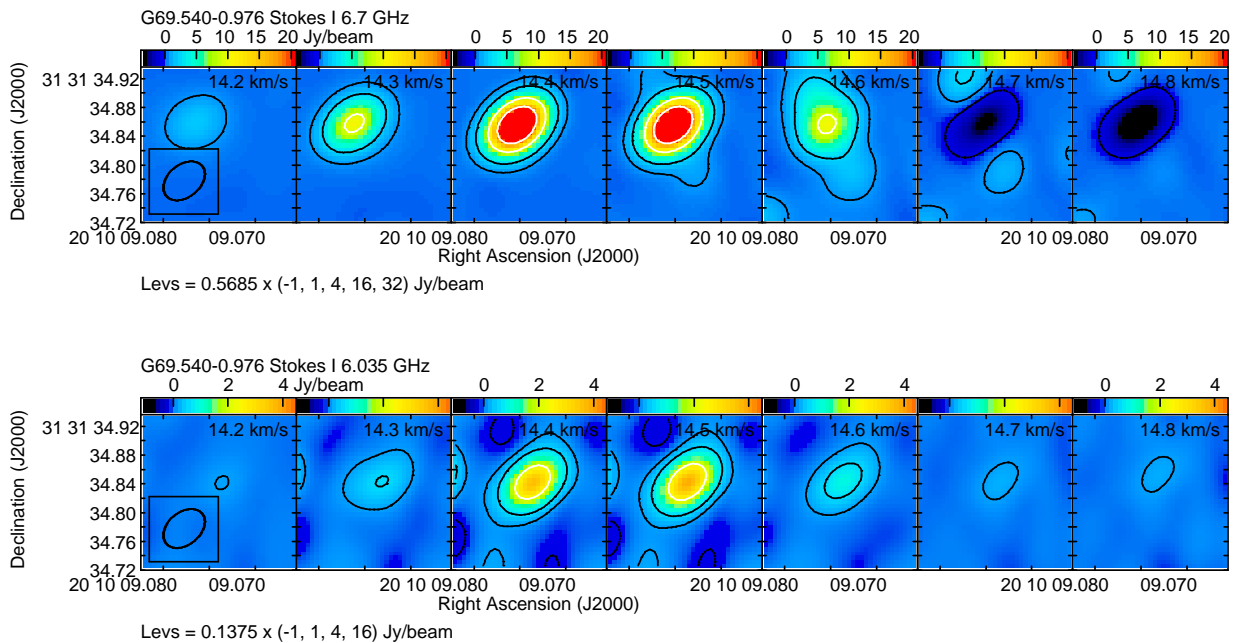


Fig. 5: Channel images showing evidence for the coexistence of 6.7 GHz methanol (top) and 6.035 GHz ex-OH (bottom) masers obtained for G69. The ex-OH emission corresponds to Zeeman pair  $Z_5$  as in Table C.1. Contours represent the emission; the first contours correspond to  $3\sigma_{rms}$  of the image, and the next contours are at 4, 8, 16,  $32\times 3\sigma_{rms}$ . The first negative contour is also shown. The numbers in the top right corner of each panel correspond to the LSR velocities of each spectral channel.

LSR velocities (see Fig. 5 as the example). In total, in these six sources, we find 12 groups of masers that are coexisting via the same gas volume. In seven cases among these 12 groups, the ex-OH shows Zeeman splitting. In more detail, in G20, G69, and G81, we find cases in which a few ex-OH and methanol spots coincide, but other regions where they are separated. In these targets, the brightest methanol spots are not associated with ex-OH emission. In G24 and G34, all ex-OH spots coexist with methanol emission, and the ex-OH masers are located in compact areas. The strongest methanol masers coexist with ex-OH masers, with spot positions within 20 mas. The two maser transitions avoid each other in the four remaining targets; that is, G25, G48, G49, and G108.

We checked correlations with other properties between areas showing the coexistence of both transitions and ones without this phenomenon. For this purpose, in all sources, we coupled the closest 6.7- and 6.035 GHz cloudlets: 12 pairs with coexistence (as was noted above) and 8 couples with avoidance. Next, we checked the following parameters for all 20 pairs: the separations of the barycenters, the velocities of the peaks, and the ratios of brightness temperatures. We note that the coincidence of both maser transitions appears for the cloudlets with their barycenters separated by less than 205 au and separations of their peak velocities below  $0.7 \text{ km s}^{-1}$ . We did not find any correlations with brightness temperature or the ratio of maximum brightness temperatures.

Based on the models by Cragg et al. (2002), the coincidence of both transitions happens when  $n_{\text{H}_2}$  is from  $10^5$  to  $10^{8.3} \text{ cm}^{-3}$ ,  $T_{\text{K}}$  is below 70 K, and  $T_{\text{D}}$  is larger than 100 K. The number densities can be calculated from the  $B_{\text{los}}$  estimated from the 37 Zeeman pairs identified (see Sect. 4.3.1 and Table C.1). In the case of four pairs (two in G108, one in G49, and one in G81),  $n_{\text{H}_2}$  exceeds a value of  $10^{8.3} \text{ cm}^{-3}$ . In fact, in all these cases, no coexistence appears for the maser lines. For the other 33 Zeeman pairs, avoidance and coincidence must be related to gas and/or dust temperatures.

In sources G20, G43, G69, and G81, there are regions of coincidence and also regions where ex-OH emission occurs without methanol transition. We have already noted that the redshifted feature ( $Z_3$ ) in G81 does not have a methanol counterpart because of the high density of the gas. In the other three sources, we know the kinetic temperature has to be below 70 K from the model. Thus, the reason for the presence of ex-OH without 6.7 GHz masers could be a decrease in the dust temperature below 100 K on scales of hundreds of astronomical units (around 500 au for G20, 1000 au for G43, and 400 au for G69).

In sources G20, G24, G34, G69, and G81, there are regions of coincidence and regions where methanol emission occurs without ex-OH transition. We know  $T_{\text{D}}$  has to be above 100 K. Thus, a possible reason for the absence of the ex-OH maser could be an increase in the kinetic temperature above 70 K, whereby the condition  $T_{\text{K}} < T_{\text{D}}$  has to be conserved. The scale of variability of  $T_{\text{K}}$  is around 170 au for G20 and G34, 1000 au for G69, and 450 au for G81.

As has been noted, in G25, G48, G49, and G108 we do not find any coexistence of the maser transitions. For G108, as for G81, we inferred a number of high densities in the volume of gas where ex-OH occurs. G25 and G49 have very bright methanol maser emission, which requires a strong IR source. From Table C.3, it can be seen that the G25 is the most massive YSO and has the highest bolometric luminosity. Hence, the main factor influencing the avoidance of both transitions in these two sources may be the distance from the YSO. In regions that are closer to the central object, and thus hotter, the 6.7 GHz maser occurs, and in distant and cooler regions, the 6.035 GHz maser transition appears. In G48, the brightness of both transitions is similar, but we observe a significant shift in the velocity domain at  $1.9 \text{ km s}^{-1}$  between methanol and ex-OH. This supports the hypothesis that these transitions appear in different volumes of gas. This target has the weakest bolometric luminosity and the smallest mass of YSO, which explains why a very weak methanol maser appeared, consisting of only two spots (Table C.3).

We find that the distributions of both masers are roughly parallel in seven targets (G24, G25, G34, G43, G49, G69, and G81),  $|\text{PA}_{6.7} - \text{PA}_{6.035}| < 31^\circ$  (Table 5). Kolmogorov-Smirnov tests for these two parameters confirm a nonrandom relationship between  $\text{PA}_{6.7}$  and  $\text{PA}_{6.035}$  values. This indicates that both masers could be associated with the same kinematic structures, although they do not necessarily trace the same parts. The blue- and redshifted maser velocities are consistent with the velocities of SO,  $\text{CH}_3\text{CN}$ , and  $\text{HC}_3\text{N}$  lines in G25, G43, and G69. That may imply that the masers arise from a disk but further data including proper motion studies are needed to verify this scenario. In Sect. 1, we pointed out that methanol masers in G69 were also considered to be associated with the outflow (Sugiyama et al. 2011). Among the other sources, we did not find signs of rotation, based on ALMA data presented in the Sect. 4.1. The masers in G24 have similar  $\text{PA}_{6.7}$  and  $\text{PA}_{6.035}$ , perpendicular to the known outflow, which may indicate a disk seen edge-on. For G34, we see a

ring-like maser morphology, but the lack of other data prevents us from determining the kinematic structure. The situation is similarly unresolved for G49 and G81. Considering the findings of the counterpart star formation tracers presented in Sect. 4.1, we notice that circular cores of millimeter dust continuum emission overlaps maser emission in G20, G24, G43, and G69. All these sources show the coincidence of both maser transitions. G43 and G69, which show more complex ex-OH emission, have much brighter 1.3 mm cores, of 159 mJy and 236 mJy, respectively, than G20 and G24, which have a brightness of 20 mJy and 3 mJy, respectively. In G49 and G81, maser emission is clearly separated from irregular millimeter cores. Those two sources are the brightest in our sample, but 6.7 and 6.035 GHz masers coexist only in G81. We cannot determine any association between kinematic structure and/or morphology and the coexistence of both maser transitions. In four sources (G24, G25, G43, and G69), masers seem to be associated with the disk, but in G25, we notice the avoidance of both maser transitions, and in the other three sources, we found partial coincidence.

Relating to our analysis of the evolutionary stages of our sample (Sect. 4.2), taking into account all three evolutionary indicators, the most evolved sources are sequentially G69, G43, and G48. All three characterize the most complex distributions of ex-OH compared to methanol masers. G69 has very bright 6.7 GHz emission,  $\sim 100 \text{ Jy}$ , but G43 and G48 are relatively weak. G69 and G43 show the coexistence of the two maser transitions, and G48 shows avoidance. We found signs of rotating disks for three sources in our sample. Among them, two are the most evolved: G69 and G43. We can also notice that, in our sample, only these three, the most evolved sources, have more complex and extended ex-OH maser structures than methanol maser structures. The next sources in the evolutionary sequence are G20, G24, G25, and G81. Three of them show coexistence, and one, G25, shows avoidance. They also have various morphologies, and only for G25 do we find the sign of a rotating disk. The last three sources, G49, G34, and G108, are in an early evolutionary phase (our interpretation for G49 could be wrong because it is not clear with which core masers emissions are associated). These sources are extremely different. G49 is the brightest source in the 6.7 GHz line in our sample and does not show a coincidence with the ex-OH line, similarly to G108, which has one of the weakest methanol maser emissions. Both sources also show a similarly complex morphology for both transitions. On the other hand, G34 shows very compact ex-OH emission, which does coincide with methanol emission.

To summarize, we do not notice a relationship between the phase of the evolution of YSO and the presence of regions with coexistence or avoidance of methanol and ex-OH masers. Some of the most evolved sources, like G43 and G69, show coincidence, but the next most evolved one, G48, shows avoidance. Also, two sources in the very early evolutionary phase, G34 and G108, show coincidence and avoidance, respectively. The factors that impact the appearance of the two transitions seem to be due to local changes in gas and dust temperatures and gas density, on the scales of a few hundred astronomical units, correlated with the distance between the maser and star and the brightness of the YSO.

## 5. Conclusions

We examined ten HMYSOs in detail, considering two maser transitions: 6.7 GHz methanol and 6.035 GHz OH. The ex-OH maser line was imaged for the first time for eight of them. The 6.7 GHz methanol maser emission is brighter than the ex-OH

line in all targets and is spread over larger regions in the sky than ex-OH masers in six of these. In three HMYSOs (G43, G48, and G69), the ex-OH masers have more complex structures and cover larger regions than methanol masers, and in one (G108) the size of both transitions is similar.

We identified regions where the two maser transitions coincided or showed avoidance. Comparing our result with archival ALMA data, we deduced that avoidance happens due to local changes in temperatures and/or densities, which are directly correlated with the brightness and distance of the masers from the YSO and not with the evolutionary stage of the HMYSO. We also attempted to identify kinematic structures, but we did not notice a correlation with the coexistence of both masers.

We detected Zeeman splitting of the ex-OH transition in eight HMYSOs, leading to magnetic field estimates of a few milligauss. In two cases, we observed a reversal of magnetic field lines along the line of sight. We detected linearly polarized ex-OH emission in nine HMYSOs and were able to compare orientations of the magnetic fields with the directions of outflows on the sky-plane, but the results are not coherent enough. We detected eight possible Zeeman triplets with two circularly polarized features at velocities bracketing a linearly polarized feature; however, observations with better angular and spectral resolution are needed to verify this result.

## Data availability

An extra appendices containing tables of polarization details, figures of masers distributions, and counterparts descriptions are available on Zenodo at: <https://doi.org/10.5281/zenodo.14865259>.

**Acknowledgements.** We acknowledge support from the National Science Centre, Poland through grant 2021/43/B/ST9/02008. We thank a referee for the very detailed and constructive revision of the manuscript. e-MERLIN is a National Facility operated by the University of Manchester at Jodrell Bank Observatory on behalf of STFC. This paper makes use of the following ALMA data: ADS/JAO.ALMA2021.1.00311.S, ADS/JAO.ALMA2019.1.00059.S, and ADS/JAO.ALMA2015.1.01596.S. ALMA is a partnership of ESO (representing its member states), NSF (USA) and NINS (Japan), together with NRC (Canada), NSTC and ASIAA (Taiwan), and KASI (Republic of Korea), in cooperation with the Republic of Chile. The Joint ALMA Observatory is operated by ESO, AUI/NRAO and NAOJ. The National Radio Astronomy Observatory is a facility of the National Science Foundation operated under cooperative agreement by Associated Universities, Inc. This work is based on observations made with the *Spitzer* Space Telescope, which is operated by the Jet Propulsion Laboratory, California Institute of Technology under a contract with NASA. This research has made use of the NASA/IPAC Infrared Science Archive, which is funded by the National Aeronautics and Space Administration and operated by the California Institute of Technology. Herschel is an ESA space observatory with science instruments provided by European-led Principal Investigator consortia and with important participation from NASA.

## References

Araya, E., Hofner, P., Kurtz, S., Bronfman, L., & DeDeo, S. 2005, *ApJS*, 157, 279  
 Avison, A., Quinn, L. J., Fuller, G. A., et al. 2016, *MNRAS*, 461, 136  
 Bartkiewicz, A., Sanna, A., Szymczak, M., et al. 2020, *A&A*, 637, A15  
 Bartkiewicz, A., Sanna, A., Szymczak, M., et al. 2024, *A&A*, 686, A275  
 Bartkiewicz, A., Szymczak, M., Cohen, R. J., & Richards, A. M. S. 2005, *MNRAS*, 361, 623  
 Bartkiewicz, A., Szymczak, M., & van Langevelde, H. J. 2014, *A&A*, 564, A110  
 Bartkiewicz, A., Szymczak, M., & van Langevelde, H. J. 2016, *A&A*, 587, A104  
 Bartkiewicz, A., Szymczak, M., van Langevelde, H. J., Richards, A. M. S., & Pihlström, Y. M. 2009, *A&A*, 502, 155  
 Baudry, A., Desmurs, J. F., Wilson, T. L., & Cohen, R. J. 1997, *A&A*, 325, 255  
 Bayandina, O. S., Alakoz, A. V., & Val'ts, I. E. 2014, *Astronomy Reports*, 58, 462  
 Caswell, J. L. & Green, J. A. 2011, *MNRAS*, 411, 2059

Cragg, D. M., Sobolev, A. M., & Godfrey, P. D. 2002, *MNRAS*, 331, 521  
 Crutcher, R. M. 1999, *ApJ*, 520, 706  
 Darwish, M. S., Richards, A. M. S., Etoka, S., et al. 2020, *MNRAS*, 499, 1441  
 Desmurs, J. F. & Baudry, A. 1998, *A&A*, 340, 521  
 Desmurs, J. F., Baudry, A., Wilson, T. L., Cohen, R. J., & Tofani, G. 1998, *A&A*, 334, 1085  
 Elia, D., Merello, M., Molinari, S., et al. 2021, *MNRAS*, 504, 2742  
 Etoka, S., Gray, M. D., & Fuller, G. A. 2012, *MNRAS*, 423, 647  
 Fish, V. L. & Reid, M. J. 2006, *ApJS*, 164, 99  
 Fish, V. L., Reid, M. J., Argon, A. L., & Zheng, X.-W. 2005, *ApJS*, 160, 220  
 Fish, V. L. & Sjouwerman, L. O. 2007, *ApJ*, 668, 331  
 Fish, V. L. & Sjouwerman, L. O. 2010, *ApJ*, 716, 106  
 Fujisawa, K., Sugiyama, K., Motogi, K., et al. 2014, *PASJ*, 66, 31  
 Garrington, S. & Beswick, R. 2016, *Astronomy and Geophysics*, 57, 3.28  
 Gaume, R. A., Johnston, K. J., & Wilson, T. L. 1993, *ApJ*, 417, 645  
 Goddi, C., Ginsburg, A., Maud, L. T., Zhang, Q., & Zapata, L. A. 2020, *ApJ*, 905, 25  
 Goddi, C., Moscadelli, L., & Sanna, A. 2011, *A&A*, 535, L8  
 Goldsmith, P. F. & Langer, W. D. 1999, *ApJ*, 517, 209  
 Green, J. A., Caswell, J. L., & McClure-Griffiths, N. M. 2015, *MNRAS*, 451, 74  
 Green, J. A. & McClure-Griffiths, N. M. 2011, *MNRAS*, 417, 2500  
 Green, J. A., Richards, A. M. S., Vlemmings, W. H. T., Diamond, P., & Cohen, R. J. 2007, *MNRAS*, 382, 770  
 Greisen, E. W. 2003, in *Astrophysics and Space Science Library*, Vol. 285, Information Handling in Astronomy - Historical Vistas, ed. A. Heck, 109  
 Hutawarakorn, B., Cohen, R. J., & Brehner, G. C. 2002, *MNRAS*, 330, 349  
 Jiménez-Donaire, M. J. 2017, PhD thesis, Ruprecht-Karls University of Heidelberg, Germany  
 Koch, P. M., Tang, Y.-W., Ho, P. T. P., et al. 2018, *ApJ*, 855, 39  
 Kumar, M. S. N., Tafalla, M., & Bachiller, R. 2004, *A&A*, 426, 195  
 McMullin, J. P., Waters, B., Schiebel, D., Young, W., & Golap, K. 2007, in *Astronomical Society of the Pacific Conference Series*, Vol. 376, *Astronomical Data Analysis Software and Systems XVI*, ed. R. A. Shaw, F. Hill, & D. J. Bell, 127  
 Moldon, J. 2021, eMCP: e-MERLIN CASA pipeline, *Astrophysics Source Code Library*, record ascl:2109.006  
 Molinari, S., Pezzuto, S., Cesaroni, R., et al. 2008, *A&A*, 481, 345  
 Molinari, S., Schisano, E., Elia, D., et al. 2016a, *A&A*, 591, A149  
 Molinari, S., Schisano, E., Elia, D., et al. 2016b, *VizieR Online Data Catalog: Hi-GAL. inner Milky Way: +68>=l>=70 (Molinari+, 2016)*, *VizieR On-line Data Catalog: J/A+A/591/A149*. Originally published in: 2016A&A...591A.149M  
 Moscadelli, L., Cesaroni, R., Rioja, M. J., Dodson, R., & Reid, M. J. 2011, *A&A*, 526, A66  
 Nagayama, T., Kobayashi, H., Omodaka, T., et al. 2015, *PASJ*, 67, 65  
 Ouyang, X.-J., Chen, X., Shen, Z.-Q., et al. 2022, *ApJS*, 260, 51  
 Pandian, J. D., Momjian, E., Xu, Y., Menten, K. M., & Goldsmith, P. F. 2011, *ApJ*, 730, 55  
 Pankonin, V., Churchwell, E., Watson, C., & Bieging, J. H. 2001, *ApJ*, 558, 194  
 Perley, R. A. & Butler, B. J. 2013, *ApJS*, 206, 16  
 Reid, M. J., Menten, K. M., Brunthaler, A., et al. 2019, *ApJ*, 885, 131  
 Richards, A. M. S., Moravec, E., Etoka, S., et al. 2022, *arXiv e-prints*, arXiv:2207.05591  
 Rosero, V., Hofner, P., Kurtz, S., Bieging, J., & Araya, E. D. 2013, *ApJS*, 207, 12  
 Rygl, K. L. J., Brunthaler, A., Reid, M. J., et al. 2010, *A&A*, 511, A2  
 Rygl, K. L. J., Brunthaler, A., Sanna, A., et al. 2012, *A&A*, 539, A79  
 Sanna, A., Moscadelli, L., Cesaroni, R., et al. 2010a, *A&A*, 517, A71  
 Sanna, A., Moscadelli, L., Cesaroni, R., et al. 2010b, *A&A*, 517, A78  
 Sato, M., Reid, M. J., Brunthaler, A., & Menten, K. M. 2010, *ApJ*, 720, 1055  
 Shi, H., Zhao, J.-H., & Han, J. L. 2010, *ApJ*, 718, L181  
 Sugiyama, K., Fujisawa, K., Doi, A., et al. 2011, *PASJ*, 63, 53  
 Sugiyama, K., Fujisawa, K., Doi, A., et al. 2008, *PASJ*, 60, 23  
 Surcis, G., Vlemmings, W. H. T., Curiel, S., et al. 2011, *A&A*, 527, A48  
 Surcis, G., Vlemmings, W. H. T., van Langevelde, H. J., & Hutawarakorn Kramer, B. 2012, *A&A*, 541, A47  
 Surcis, G., Vlemmings, W. H. T., van Langevelde, H. J., Hutawarakorn Kramer, B., & Bartkiewicz, A. 2019, *A&A*, 623, A130  
 Surcis, G., Vlemmings, W. H. T., van Langevelde, H. J., Hutawarakorn Kramer, B., & Bartkiewicz, A. 2022, *A&A*, 658, A78  
 Surcis, G., Vlemmings, W. H. T., van Langevelde, H. J., et al. 2015, *A&A*, 578, A102  
 Surcis, G., Vlemmings, W. H. T., van Langevelde, H. J., Hutawarakorn Kramer, B., & Quiroga-Núñez, L. H. 2013, *A&A*, 556, A73  
 Szymczak, M., Wolak, P., Bartkiewicz, A., Aramowicz, M., & Durjasz, M. 2020, *A&A*, 642, A145  
 Torrelles, J. M., Gómez, J. F., Rodríguez, L. F., et al. 1997, *ApJ*, 489, 744  
 Vlemmings, W. H. T. 2008, *A&A*, 484, 773  
 Vlemmings, W. H. T., Torres, R. M., & Dodson, R. 2011, *A&A*, 529, A95  
 Wilson, T. L. & Rood, R. 1994, *ARA&A*, 32, 191  
 Wrobel, J. M. & Walker, R. C. 1999, in *Astronomical Society of the Pacific Conference Series*, Vol. 180, *Synthesis Imaging in Radio Astronomy II*, ed. G. B. Taylor, C. L. Carilli, & R. A. Perley, 171  
 Xu, Y., Reid, M. J., Menten, K. M., et al. 2009, *ApJ*, 693, 413  
 Zhang, B., Reid, M. J., Menten, K. M., et al. 2013, *ApJ*, 775, 79

## Appendix A: Methyl cyanide

Methyl cyanide ( $\text{CH}_3\text{CN}$ )  $J = 12 - 11$  rotational transition could be analyzed for a number of sources using the data from the ALMA Science Archive. Under the assumption that the lines are optically thin, a rotational temperature can be derived from the line intensities of various  $K$  components. If the lines are optically thick, the various  $K$  intensities versus the upper energy level will deviate from a linear slope, and the slope may flatten, which leads to overestimated temperatures (Goldsmith & Langer 1999). When also the  $^{13}\text{C}$  isotopolog,  $\text{CH}_3^{13}\text{CN}$ , is detected, the optical depth of  $\text{CH}_3^{12}\text{CN}$  can be derived from the  $K$  line intensity ratio under the assumptions that  $\text{CH}_3^{13}\text{CN}$  is optically thin and the  $^{12}\text{C}/^{13}\text{C}$  line ratio of 50 (Wilson & Rood 1994). See Jiménez-Donaire (2017) for a detailed explanation.

Following the analysis outlined in Pankonin et al. (2001), Araya et al. (2005) and Rosero et al. (2013) we analyzed available ALMA archival data. We used eight Gaussians to fit contemporaneously the  $K = 0$  to  $K = 7$  components, constraining the line width of all lines to be the same as for the bright and unblended  $K = 3$  component, and fixing positions of the lines to the rest frequencies, after taking into account the LSR velocity of the target. The results of the fits are given in Table A.1.

Strong deviations from linear were found for G20 and G25, less so for G43, and least for G69. Since also the  $K = 2$   $\text{CH}_3^{13}\text{CN}$  could be detected, the optical depth of the main isotopolog ( $\tau_{12\text{C}}$ ) could be calculated. We find that  $\text{CH}_3^{12}\text{CN}$  is indeed optically thick for all our sources, more so for those with a stronger deviation from linear. Therefore, all of our estimated temperatures are overestimated, and our column densities are underestimated. On the argument of beam dilution, which is often invoked in the past single-dish analysis of  $\text{CH}_3\text{CN}$ , we are less worried because we use ALMA interferometric data. We measured the spectra in ellipses chosen to include most of the  $\text{CH}_3\text{CN}$  emitting core which overlapped or was closest to the maser emitting region. The smallest minor axis was 0.4 arcsec and the largest major axis was 1.2 arcsec, these being (slightly) larger than the beam sizes. The emission of the  $\text{CH}_3\text{CN}$   $J = 12 - 11$  transition observed by ALMA is thus slightly extended, making it plausible to use a beam filling factor of unity.

Table A.1: Derived parameters of the  $\text{CH}_3\text{CN}$   $J = 12 - 11$  ALMA observations.

Source	vlsr ( $\text{km s}^{-1}$ )	linewidth ( $\text{km s}^{-1}$ )	$\int T\delta v$ ( $\text{K km s}^{-1}$ )								Trot K	N ( $\text{e}^{14} \text{cm}^{-2}$ )	$^{13}\text{C}$ ratio	$\tau_{12\text{C}}$	
			$K = 0$	$K = 1$	$K = 2$	$K = 3$	$K = 4$	$K = 5$	$K = 6$	$K = 7$					
G20	72.5	3.4	87.5	80.2	87.9	91.2	55.4	50.6	43.2	21.9	335(79)	25.1(3.8)	y	7.7	6.5
G25	42.0	4.2	456.9	491.1	514.6	566.4	407.0	345.9	362.6	150.4	446(143)	229(32)	y	7.6	6.5
G43	12.0	2.1	37.4	30.4	28.9	31.6	14.8	9.3	9.5	3.4	177(15)	4.4(0.5)	y	8.4	5.9
G69	14.0	1.7	167.3	155.2	145.1	162.2	95.1	64.7	56.8	14.5	180(18)	23.7(2.9)	y	14.8	3.4